Primary droplet formation in a microscopic vibrating-mesh nebulizer aperture at ultrasonic frequency: Computational and macroscale experimental modeling

Mohsen H. Moghimi ; José A. Monterrubio López; Ciarán Guy ; Gerard M. O'Connor ; Ronan MacLoughlin ; Nathan J. Quinlan ✉

Check for updates

View Online

Export Citation

Articles You May Be Interested In

Pulmonary monoclonal antibody delivery via a portable microfluidic nebulization platform

Biomicrofluidics (April 2015)

Portable acoustofluidic nebulizer

J. Acoust. Soc. Am. (October 2019)

Intelligent airflow of nebulizer using IoT-based circuit integration for smart healthcare management

AIP Conf. Proc. (December 2023)

AIP Publishing

Physics of Fluids

Special Topics Open for Submissions

Learn More

AIP Publishing

Primary droplet formation in a microscopic vibrating-mesh nebulizer aperture at ultrasonic frequency: Computational and macroscale experimental modeling

Mohsen H. Moghimi,[1,2,a)] (iD) José A. Monterrubio López,[1,2] Ciarán Guy,[2,3] (iD) Gerard M. O'Connor,[2,3] (iD)
Ronan MacLoughlin,[4] (iD) and Nathan J. Quinlan[1,2,b)] (iD)

AFFILIATIONS

[1]School of Engineering, University of Galway, Galway H91 TK33, Ireland
[2]CÚRAM Centre for Research in Medical Devices, Galway H91 TK33, Ireland
[3]School of Natural Sciences, University of Galway, Galway H91 TK33, Ireland
[4]Aerogen Ltd., Galway H91 HE94, Ireland

[a)]Present address: Pharmaceutical Manufacturing Technology Centre, University of Limerick, Limerick V94 T9PX, Ireland.
[b)]Author to whom correspondence should be addressed: nathan.quinlan@universityofgalway.ie

ABSTRACT

Vibrating-mesh nebulizers (VMNs) generate inhalable aerosols of liquid therapeutic agents. The aerosol is generated by vibration of a mesh plate with many microscopic apertures. The objective of this work is to understand the mechanisms of flow through the apertures and the formation of primary aerosol droplets. The flow was simulated computationally using the meshless finite volume particle method with the approximation of axisymmetric single-phase flow. For validation, a large-scale model aperture of 0.5 mm diameter was designed, with liquid properties and oscillation parameters scaled to approximate the Reynolds and Weber numbers of the flow from a microscopic aperture of a VMN device. Computations and experiments show that liquid is pressurized by motion of the aperture plate, and consequently pumped through the aperture. The resulting jet breaks up under Plateau–Rayleigh-like capillary instability. This leads to the formation of multiple droplets on each oscillation cycle of the aperture plate, with droplet diameter on the order of aperture diameter. After primary breakup, some new droplets are formed by coalescence of colliding droplets and jets, and as satellite drops in breakup events. Experiments and computations agree on the structure of the flow. In the VMN device, the oscillation period of the VMN aperture plate is on the order of the time taken for acoustic waves to propagate across the system. Consequently, liquid compressibility plays an important role in pumping. The model may be enhanced in future work to remove the restriction to axisymmetric flow and include interaction of the liquid with the air phase.

I. INTRODUCTION

In this article, we present an investigation of fluid mechanics of aerosol droplet formation in vibrating-mesh nebulizers (VMN). VMNs generate aerosols of liquid medication for drug delivery by inhalation. They have been used successfully in a range of clinical applications, including neonatal care,[1] intensive care,[2] and COVID-19 vaccination.[3] They deliver a higher fraction of payload to the lung than alternative technology in both adults[4] and neonatal models.[1,5] They are safe for use with therapies that are sensitive to high temperature

and shear stress[6] and can readily be installed in a mechanical ventilator or configured in a hand-held device for home use. Reviews of aerosol therapy technology, including VMNs, are provided by Watts *et al.*[7] and Arnott *et al.*[8]

A VMN device includes a vibrating mesh or aperture plate, typically 5–10 mm in diameter, with approximately 1000 apertures of several micrometers in diameter. The plate is excited by a piezoelectric actuator in oscillatory elastic deformations, near resonance, at ultrasonic frequency. Liquid therapeutic agent is retained in a reservoir

above the plate. As a result of plate oscillation, liquid is pumped through the apertures to emerge as a droplet aerosol, as shown schematically in Fig. 1. The reservoir is vented to the atmosphere and the downstream side is connected to the mouthpiece of a hand-held device or the breathing circuit of a mechanical ventilator. The therapeutic function of the device is strongly dependent on the aerosol droplet size distribution, and the volume of agent aerosolized.

The objective of the present work is to develop understanding of the fluid mechanics of the technology at the level of a single microscopic aperture. Experimental access is difficult because of the microsecond and micrometer scales, embedded within a device measuring tens of millimeters. Therefore, we use a computational approach. Conceptually, as discussed in Sec. II and illustrated in Fig. 1, the mechanics can be separated into a pumping process, which drives flow through the apertures, and a downstream droplet formation process. We have developed a scaled-up experimental model which operates at Reynolds and Weber numbers, representative of the microscopic VMN aperture (Sec. III). Flow in this large-scale model was visualized experimentally and simulated computationally to validate the computational model. Following validation, flow in the microscale VMN aperture was simulated without any scaling. All computational simulations were carried out for a domain around one VMN aperture, using the meshless finite volume particle method (FVPM). Flow is approximated as axisymmetric and single-phase. Computational methods are described in Sec. IV. Numerical and experimental results are presented in Sec. V, including a comparison of experimental and computational results for validation purposes.

II. MODEL DEFINITION AND THEORETICAL CONSIDERATIONS

In our model, we consider a single aperture of diameter $D = 4$ μm in the aperture plate of a vibrating mesh system, with geometry representative of an Aerogen® VMN, as shown in Fig. 1. The circular plate is clamped around its circumference and undergoes elastic oscillations, with deflection on the order of 10^{-3} plate diameters normal to the plate, based on vibrometry provided by the manufacturer. At the

FIG. 1. Schematic diagram of VMN apertures in operation.

scale of the whole plate, the non-uniform oscillation must induce some transverse multidimensional flow in the reservoir. However, over a microscopic region of interest spanning one or a small number of apertures, the very small normal deflection indicates that the plate is flat and its motion is uniform, to a very good approximation. The dominant effect of this motion on the fluid, in the local region, is displacement of fluid normal to the plate.

To simulate flow in this framework, the domain is a cylindrical region, extending above and below the aperture plate, centered on one aperture. Oscillatory plate motion is parallel to the centerline of the aperture (vertical in the diagram). Transverse motion of the fluid through the vertical outer boundaries of the cylindrical domain is neglected, and those boundaries are treated as free-slip walls. The free surface of the liquid in the reservoir is outside the domain, up to tens of millimeters (thousands of aperture diameters) above. This depth decreases as the reservoir is depleted. Only the liquid phase is modeled. Within this framework, we now apply theoretical and existing empirical knowledge to the pumping and droplet formation processes.

A. Pumping

For the purposes of this discussion of mechanics in the reservoir, the aperture area is considered very small in comparison with the reservoir area, so that flow through the aperture is negligible in comparison with bulk displacement of liquid in the reservoir. First, we consider the limiting case of incompressible liquid. The bulk incompressible liquid in the reservoir must oscillate vertically with the displacement of the plate, denoted $z_p(t)$. The pressure required at the plate surface to accelerate the liquid is $p(t) = -\rho \ddot{z}_p(t)(H - h)$, where H is the height of the free surface above the aperture exit ($z = 0$) and h is the thickness of the plate. Since $z_p(t) = A \sin(2\pi f t)$, where A is displacement amplitude and f is frequency, the maximum pressure is $\rho A (2\pi f)^2 (H - h)$. For order-of-magnitude values of amplitude $A \simeq 1$ μm, frequency $f \simeq 100$ kHz, and $H \simeq 10$ mm, the expected pressure amplitude is approximately 4 MPa.

Incompressibility implies infinite sound speed. However, effects of aperture plate motion propagate through the liquid by acoustic waves at the finite speed of sound. For $H \simeq 10$ and sound speed $c \simeq 1500$ m/s for water, an acoustic wave transits from the plate to the liquid free surface in approximately 7 μs, which is on the order of the oscillation period at ~ 100 kHz. Before a compression wave from upwards acceleration of the plate reaches the free surface, the plate has reversed direction. Therefore, the liquid column cannot reach an equilibrium hydrostatic pressure distribution, and the pressure field in the reservoir is dominated by unsteady waves. Therefore, the finite sound speed is significant, and compressibility must be considered. The pressure resulting from impulsive start of a plate at velocity $\dot{z}_p$ with speed of sound c is given by $p = \rho \dot{z}_p c$. Taking $\dot{z}_p$ as the maximum plate velocity $A\omega$, the maximum pressure is estimated on the order of 1 MPa. In contrast with the incompressible case, this estimate is determined by local compression of the liquid just above the plate, rather than acceleration of the bulk liquid. If reservoir depth is small and/or frequency is low, the compressible model may approach the incompressible approximation.

Thus, upward acceleration of the aperture plate, against the inertia of the liquid, provides the high pressure, which can pump liquid through the aperture. In the compressible regime, compressive acoustic waves are the mechanism for pressurization. In the incompressible
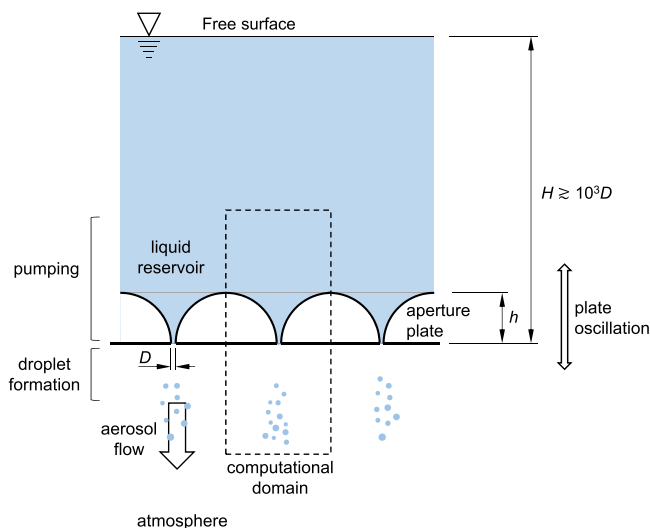
regime (which is relevant for the large-scale model, described in Sec. III), the plate must accelerate the whole liquid column. Flow through the aperture will modify the pumping mechanism itself, but as aperture exit area is on the order of 0.1% of plate area, this is not expected to fundamentally alter these mechanisms.

B. Droplet formation

The pumped liquid emerges from the aperture as a jet into air. Following von Ohnesorge,[9] the literature conventionally classifies jet breakup regimes in terms of the jet Reynolds and Ohnesorge numbers.[10,11] These are $Re_D = \rho U D / \mu$ and $Oh = \mu / (\sigma \rho D)^{1/2}$, respectively, where σ is surface tension coefficient, μ is liquid dynamic viscosity, ρ is liquid density, and D is jet diameter. The Ohnesorge number can also be expressed as to $\sqrt{We}/Re_D$, in terms of the Weber number $We = \rho U^2 D / \sigma$.

The classical Ohnesorge diagram provides a map of jet breakup behavior in the Re_D-Oh plane, based on theoretical and empirical work, summarized for example by Trettel.[12] For a given liquid and liquid-gas density ratio (corresponding to water and air in the present work), regime boundaries can be defined solely in terms of the liquid Weber number. Dripping flow is expected for $We = \rho U^2 D / \sigma \lesssim 8$. For $8 \lesssim We \lesssim 330$, breakup is dominated by capillary instability, defining the Rayleigh regime. The so-called first and second wind-induced breakup regimes begin at $We \simeq 330$ and $We \simeq 11\,000$, respectively. These much-cited regime boundaries have been subject to recent criticism,[12] but may provide useful indications.

For representative VMN conditions, with a water-based liquid jet of diameter $D = 4~\mu m$ in air, the Rayleigh regime of $8 \lesssim We \lesssim 330$ corresponds to jet velocity in the range $10~m/s \lesssim U \lesssim 80~m/s$. In this range, perturbations in an initially cylindrical liquid column grow under a capillary instability, in a linear manner at first, finally leading to pinch-off and droplet formation. Rayleigh[13] predicted the wavelength λ_0 of the fastest-growing perturbation as $\lambda_0 / D = 4.508$. Weber incorporated viscous effects[14] to obtain

$$\frac{\lambda_0}{D} = \pi (2 + Oh \sqrt{18})^{1/2}, \quad (1)$$

where $Oh = \mu / (\sigma \rho D)^{1/2}$ is the Ohnesorge number. This gives $\lambda_0 / D = 4.710$ for water ($Oh = 0.0583$), or $\lambda_0 / D = 4.443$ in the inviscid limit. Assuming that each full wavelength of this fastest-growing mode leads to one droplet, and the liquid column remains sinusoidal until breakup, droplet diameter d can be estimated as

$$\frac{d}{D} = \left(\frac{3\lambda_0}{2D}\right)^{1/3}, \quad (2)$$

giving $d/D = 1.92$ for water. This is an estimate of droplet size, assuming jet breakup occurs in the Rayleigh regime.

III. EXPERIMENTAL METHOD

A large-scale experimental model was developed to inform the qualitative understanding of jet breakup and validate the computational model. The model represents one aperture of the vibrating mesh, scaled up to time and length scales that facilitate direct imaging of droplet formation. The model was designed with dimensional analysis to ensure that physical phenomena in microscale droplet formation are properly represented in the scaled-up model. The experimental

model is not expected to replicate the microscale process, but to serve as a test of the computational model in a representative operating regime.

A. Dimensional analysis for design of experimental model

The scope of the present work excludes liquid-air interaction effects so that in the space of possible scaled-up designs, performance is a function only of liquid properties, aperture geometry, and oscillation. The dependence of droplet diameter (or any performance variable) on model design can be expressed as

$$d = d(D, f, A, g, \rho, \mu, \sigma, c), \quad (3)$$

where D is aperture exit diameter, f is plate vibration frequency, A is plate vibration amplitude (from mean to peak displacement), and g is acceleration due to gravity. Fluid properties ρ, μ, σ, and c are liquid density, viscosity, surface tension coefficient, and speed of sound, respectively. According to the Buckingham Pi theorem, the nine variables of Eq. (3), in three base dimensions (length, time, and mass), may be reduced to $9-3 = 6$ dimensionless groups.

A convenient choice of dimensionless groups is

$$\frac{d}{D} = d^* = d^* \left(\frac{\rho (2\pi f A) D}{\mu}, \frac{\rho g D^2}{\sigma}, \frac{\rho (2\pi f A)^2 D}{\sigma}, \frac{(2\pi f A)}{c}, A/D \right), \quad (4)$$

where the first four groups on the right-hand side are the Reynolds, Bond, Weber, and Mach numbers, respectively, based on aperture diameter D and peak plate velocity $2\pi f A$. To achieve similarity between the microscopic VMN aperture and the macroscale model, the independent dimensionless design variables should be matched in each. They can be manipulated in design of the macroscale system by adjusting frequency, amplitude, and viscosity over wide ranges. However, the other fluid properties, ρ, σ, and c, have much more limited ranges, and g is difficult to adjust. The choice of diameter D is limited by our requirement to have a practical scale for experimental visualization. This leaves only three free variables—f, A, and μ—with which to match five dimensionless numbers. Furthermore, at the desired $D \simeq 0.5$ mm, the liquid reservoir depth would scale impractically to multiple meters. Thus, complete similarity cannot be achieved.

These problems can be avoided by recognizing that droplet formation mechanics depends primarily on properties of the jet, and only indirectly on the pumping process that generates the jet. Therefore, we limit the scope of the large-scale experiment to the droplet formation process downstream of the aperture. The jet can be characterized by peak aperture exit velocity U along with f and D. The functional dependence then reads

$$d = d(D, f, U, g, \rho, \mu, \sigma), \quad (5)$$

non-dimensionalized as

$$\frac{d}{D} = d^* = d^* \left(\frac{\rho U D}{\mu}, \frac{\rho g D^2}{\sigma}, \frac{\rho U^2 D}{\sigma}, \frac{f D}{U} \right)$$
$$= d^* (Re, Bo, We, St). \quad (6)$$

Dimensionless droplet size depends on the Reynolds number Re, the Bond number Bo, the Weber number We, and the Strouhal number St. Further simplification is possible since $Bo \lesssim 10^{-5}$ in the

microscale aperture, indicating that gravity is negligible in comparison with capillary effects. Therefore, it is not necessary for the model to exactly match the microscale Bond number, as long as Bo remains small. Thus, setting $D = 0.5$ mm to facilitate imaging in the large-scale model, we can select U, μ, and f to achieve an acceptable match for Re, We, and St.

Jet velocity U depends on the pumping oscillation amplitude A, which was set by an iterative process, using the computational models of the micro- and large-scale apertures, as described in Sec. IV. Practically, it is also required that gravity must not overcome surface tension at the aperture exit in hydrostatic conditions. The maximum depth for this criterion is approximately 60 mm. Reservoir depth in the large-scale model is therefore set at 15 mm, twice the aperture plate thickness.

The resulting dimensionless parameters of the VMN and large-scale model are listed in Table I, based on computational models of both (described in detail below in Sec. IV). The effective geometric scale factor of the model aperture, with respect to a microscopic VMN aperture, is 125. In the final design, Re_D and We_D in the large-scale model are approximately 1/2 and 1/5 of the respective values in the VMN. Although an exact match was not possible, the low Weber number in both cases suggests operation in the dripping or Rayleigh regimes. The scale model can therefore be used to validate the computational model in operating regime representative of the microscopic VMN.

In the dripping and Rayleigh regimes, predicted by low Weber number, breakup is well modeled by theory based on capillary effects, without interaction forces due to the gas phase. Estimated aerodynamic drag force on a droplet at VMN scale would cause the velocity to decrease by less than 10% over the modeled travel distance of 100 aperture diameters. These estimates support the omission of the air phase as an approximation for the purposes of this investigation.

With a reservoir depth of 15 mm in the large-scale model, a sound wave travels from the aperture exit to the upper free surface in approximately 10 μs, orders of magnitude less than the oscillation period of around 0.012 s. This makes it possible for a quasi-steady hydrostatic pressure distribution to evolve, governed by the instantaneous acceleration of the plate. Thus, the pumping mechanism is essentially incompressible in the large-scale model, in contrast with the microscale VMN.

B. Experimental model and apparatus

The model aperture is shown in Fig. 2. The aperture, of exit diameter 0.5 mm, is a nozzle located in the floor of a vessel which models
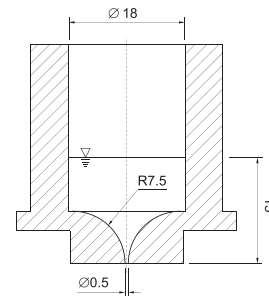

FIG. 2. Sectioned view of the scaled-up experimental model of a VMN aperture. Dimensions in mm.

the column of liquid above a single VMN aperture. The top of the vessel is vented to the atmosphere. The vessel is machined from polyacetal and mounted on a MGV52 voice-coil actuator with AKB3-G-WHI 5/100SE-T2 controller (Akribis Systems, Singapore), which drives oscillation at 83 Hz with an amplitude of 0.215 mm. A Phantom v310 camera (Vision Research, New Jersey, USA) with a 135 mm Nikon photographic lens was used to image the flow at 3140 fps. The field of view measures 50 mm from the aperture exit downstream and 30 mm wide. The reservoir is filled to a depth of 15 mm above the aperture exit with a 40/60 water/glycerol mixture of viscosity 0.010 Pa · s and surface tension coefficient 0.066 N m^{-1}.

IV. COMPUTATIONAL METHODS

To assist in resolving complex dynamic free surfaces in droplet formation, we use a particle-based numerical method to discretize the Navier–Stokes equations. Such methods, exemplified by smoothed particle hydrodynamics (SPH), are suitable for the present application because they track the free surface straightforwardly with Lagrangian particles.[15,16] In particular, we use the finite volume particle method (FVPM), derived from SPH. The method is outlined in Sec. IV A, and specific methods for the VMN application are presented in Secs. IV B and IV C.

A. The finite volume particle method

In the finite volume particle method (FVPM),[17–19] fluid is discretized by computational particles which move at arbitrary velocity (typically chosen equal to local fluid velocity). Each particle i is associated with a compactly supported weight function $W_i(\mathbf{x}, t) = W(\mathbf{x} - \mathbf{x}_i(t), h_i)$, where W is a generic kernel shape and $2h$ is the radius of

TABLE I. Dimensionless parameters of the microscopic VMN and large-scale experimental model, based on mean jet velocity in computational models of each.

Dimensionless number	Symbol	Definition	VMN	Large-scale model
Reynolds	Re_D	$\rho U D/\mu$	50.9	24.4
Weber	We_D	$\rho U^2 D/\sigma$	8.80	1.64
Amplitude	$\cdots$	A/D	0.31	0.43
Strouhal	St	fD/U	0.0403	0.0935
Bond	Bo	$\rho g D^2/\sigma$	2.1×10^{-6}	0.041
Mach	M	U/c_0	8.6×10^{-3}	0.30×10^{-3}
Contact angle (aperture surface)	θ_c	$\cdots$	105°	76°

the compact support. This is normalized with respect to weight functions of neighboring particles j to construct a test function

$$\psi_i(\mathbf{x}, t) = \frac{W_i(\mathbf{x}, t)}{\sum_j W_j(\vec{x}, t)}, \tag{7}$$

with the property $\sum_i \psi_i(\mathbf{x}, t) = 1$. This is used to smooth the governing equations, here written in general form with conserved variables $\mathbf{U}$ and flux $\mathbf{F}$,

$$\frac{\mathrm{d}}{\mathrm{d}t} \int_\Omega \psi_i(\mathbf{x}, t) \mathbf{U} \mathrm{d}\mathbf{x}$$
$$- \int_\Omega \left(\nabla \psi_i(\mathbf{x}, t) \cdot \mathbf{F}(\mathbf{U}) + \mathbf{U} \frac{\partial \psi_i}{\partial t} \right) \mathrm{d}\mathbf{x}$$
$$+ \int_{\partial\Omega} \psi_i(\mathbf{x}, t) \mathbf{F}(\mathbf{U}) \cdot \mathbf{n} \mathrm{d}S = 0. \tag{8}$$

Evaluation of the spatial integrals in Eq. (8) is a defining feature of FVPM. Domains of integration are partitioned into particle overlap regions, and $\mathbf{U}$ and $\mathbf{F}$ are approximated as uniform within these regions, so that integrands involve only the known weight functions W_i. This yields

$$\frac{\mathrm{d}}{\mathrm{d}t}(V_i \mathbf{U}_i) + \sum_j \boldsymbol{\beta}_{ij} \cdot \boldsymbol{\mathcal{G}}(\mathbf{U}_i, \mathbf{U}_j, \dot{\mathbf{x}}_i, \dot{\mathbf{x}}_j) + \boldsymbol{\beta}_i^b \cdot \boldsymbol{\mathcal{G}}_i^b = 0, \tag{9}$$

where each j denotes a particle neighboring i, particle volume $V_i = \int_\Omega \psi_i(\mathbf{x}, t) \mathrm{d}\mathbf{x}$, interparticle area $\boldsymbol{\beta}_{ij} = \boldsymbol{\gamma}_{ij} - \boldsymbol{\gamma}_{ji}$, and

$$\boldsymbol{\gamma}_{ij} = \int_\Omega \frac{W_i(\mathbf{x}) \nabla W_j(\mathbf{x})}{\left(\sum_k W_k(\mathbf{x}) \right)^2} \mathrm{d}\mathbf{x}. \tag{10}$$

The numerical flux function $\boldsymbol{\mathcal{G}}(\mathbf{U}_i, \mathbf{U}_j, \dot{\mathbf{x}}_i, \dot{\mathbf{x}}_j)$ approximates the flux $\mathbf{F}(\mathbf{U})$, accounting for transport due to relative particle velocity $\dot{\mathbf{x}}_i - \dot{\mathbf{x}}_j$, and is typically computed with an approximate Riemann solver. The superscript b denotes boundary terms. There is a rigorous analogy with the classical finite mesh-based volume method (FVM), with $\boldsymbol{\beta}_{ij}$ and $\boldsymbol{\beta}_i^b$ corresponding to cell–cell and cell–boundary interface areas, respectively.[18] Like FVM, FVPM ensures exact conservation because $\boldsymbol{\beta}_{ij} = -\boldsymbol{\beta}_{ji}$ and consistency because $\sum_j \boldsymbol{\beta}_{ij} = 0$.

The choice of weight function is critical for the accuracy and cost of the method. We define $W_i(\mathbf{x})$ as 1 inside the support of particle i and 0 elsewhere. This enables exact computation of integrals such as Eq. (10) for $\boldsymbol{\beta}_{ij}$ and V_i, in turn ensuring the conservation and consistency properties mentioned above. It also greatly reduces computational cost in comparison with numerical integration of polynomial weight functions.[20] Additional details and analysis are given by Hietel et al.[17] and Nestor et al.[21]

B. Application-specific details

In the present work, we model the problem as axisymmetric. Rather than a sphere or disk, each particle is a sector of a torus, formed by revolving a disk through a small angle about the z axis.[22,23] Geometric calculations such as (10) operate in a 2D space but must be modified slightly from the Cartesian form. Unbalanced tangential pressure and surface tension forces result in additional radial forces.
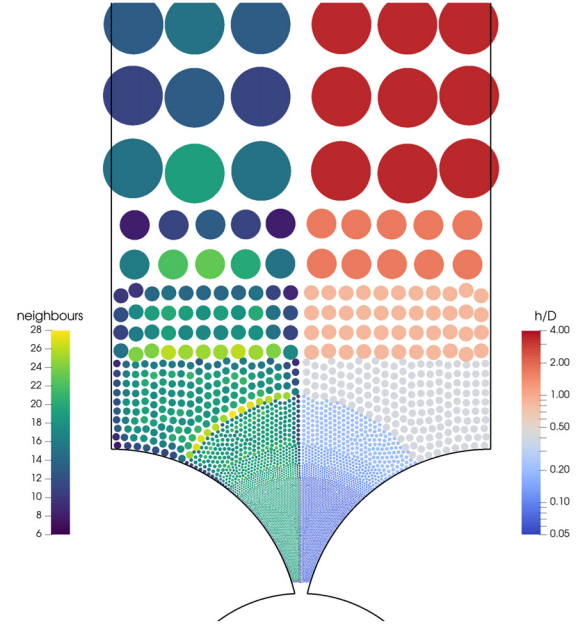

FIG. 3. Initial particle distribution, illustrated for a coarse particle spacing Δx of $D/\Delta x = 8$, colored by (left) number of neighbor particles and (right) particle smoothing length h (half of particle radius), normalized to aperture exit diameter D.

Particles are initialized with non-uniform size and spacing, to maintain adequate spatial resolution in the aperture, jet, and droplets, while reducing resolution and computational effort in the reservoir. An example of initial particle distribution is shown in Fig. 3 for a low-resolution case of eight particles across the aperture exit diameter.

Particles are moved with nearly Lagrangian velocity (i.e., $\dot{\mathbf{x}}_i = \mathbf{u}_i + \dot{\mathbf{x}}_i'$), where $\dot{\mathbf{x}}_i'$ is a relatively small arbitrary Lagrangian–Eulerian (ALE) numerical particle velocity shift to maintain smooth uniform particle distribution.[24] Lagrangian continuum elements change their area in the $r - z$ plane as they move radially, to maintain constant volume. Consequently, numerical particles move apart when they move toward the axis, leading to reduced particle number density despite nearly constant fluid density. To prevent the consequent
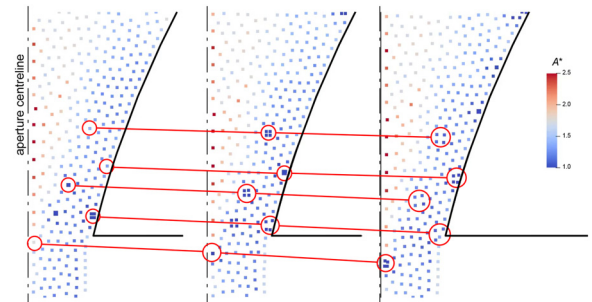

FIG. 4. Sequence of particle distribution in the aperture, highlighting the splitting and shifting of particles to avoid numerical voids near the axis, colored by A^*, the normalized inverse particle number density.

development of numerical voids, particles with low number density and large negative radial velocity are split into four new clone particles, of equal size to the original particle.[22] The new particles are initially positioned very near the original particle, but drift apart in ALE motion under the particle shifting scheme. In practice, this is needed only inside the aperture nozzle. An illustration of this splitting procedure is shown in Fig. 4.

The flux $\mathcal{G}$ is computed with the AUSM$^+$-up Riemann solver,[25] with consistency-corrected SPH approximations[26] to compute gradients, and the Barth–Jespersen slope limiter,[27] for formal second-order accuracy. The physical free surface is identified by segments of particle support boundaries that are not covered by other particles. Surface tension forces are applied between pairs of such free surface particles, and between free surface particles and the wall, accounting for the prescribed equilibrium contact angle.[28] Atmospheric pressure p_a is also applied on these segments, usually at a level of 1 MPa to suppress spurious numerical voids.[29] Results are insensitive to the value of this background pressure. This method has previously been validated by Moghimi and Quinlan[23] and Moghimi[30] for canonical Plateau–Raleigh instability and breakup of steady jets in dripping and Rayleigh regimes.

C. Geometry, boundary conditions, and fluid properties

The geometry of the computational models is shown in Fig. 5 for both the microscopic VMN aperture [Fig. 5(a)], which is representative of Aerogen® devices, and the large-scale experimental model [Fig. 5(c)], which is somewhat simplified. In addition, to investigate aspects of the pumping process, we model a reservoir bounded by a solid plate without an aperture [Fig. 5(b)] with a domain of similar dimensions to the microscopic VMN aperture. Geometry is assumed axisymmetric and only half of the 2D geometry shown is modeled in each case. In these diagrams and in results, the geometry is mirrored to provide a symmetric visualization.

The governing equations are formulated in a reference frame fixed to the local aperture plate. Defining the plate displacement as $z_p(t) = -A\sin(\omega t)$, its acceleration is $\ddot{z}_p(t) = A\omega^2\sin(\omega t)$. A body force per unit mass of $A\omega^2\sin(\omega t)$ is therefore applied.

The physical surfaces of the aperture plate are modeled as no-slip walls. The cylindrical outer boundary of the domain is modeled as a free-slip wall, except in the large-scale model, where it is the no-slip wall representing the physical wall of the vessel. The lower boundary is an outlet.

In the computational model of the microscopic VMN, it would be costly to model the whole reservoir, which extends for thousands of aperture diameters in every direction. Instead, the upper boundary must represent the interaction of the small computational domain with the distant bulk fluid. We implement a boundary condition through which characteristic waves propagate to the far field, while waves from the free surface, far above, propagate inwards. Based on the 1D Euler equation for flow normal to the boundary, the Riemann invariants

$$J_+ = u_z(z) + p(z)/(\rho c),\qquad(11)$$

$$J_- = u_z(z) - p(z)/(\rho c)\qquad(12)$$

are propagated outward $(+z)$ and inward $(-z)$, respectively, with constant value. J_+ can be determined from field values at points just inside the boundary—in practice, at the particles closest to the boundary. In the far field, at the free surface, the vertical velocity is approximately zero (in the absolute frame) and the pressure is atmospheric pressure p_a, giving $J_- = -p_a/(\rho c)$. With known J_+ and J_-, Eqs. (11) and (12) can be solved for u_z and p at the boundary, which in turn can be used to calculate boundary fluxes. Care is required to convert u_z into the oscillating reference frame. Numerical tests confirmed that results are unaffected by the boundary position, as long as the domain height is greater than approximately $50D$.

In the large-scale model, the reservoir can be modeled in full and the upper free surface is simulated directly. The model is initialized with liquid up to the depth in the experiment.

The modified Tait equation of state (EoS) $p - p_a = (\rho_0 c_0^2/\gamma)[(\rho/\rho_0)^\gamma - 1]$ is used with $\gamma = 7$, where ρ_0 and c_0 are the density and speed of sound, respectively, at the pressure p_a. This equation
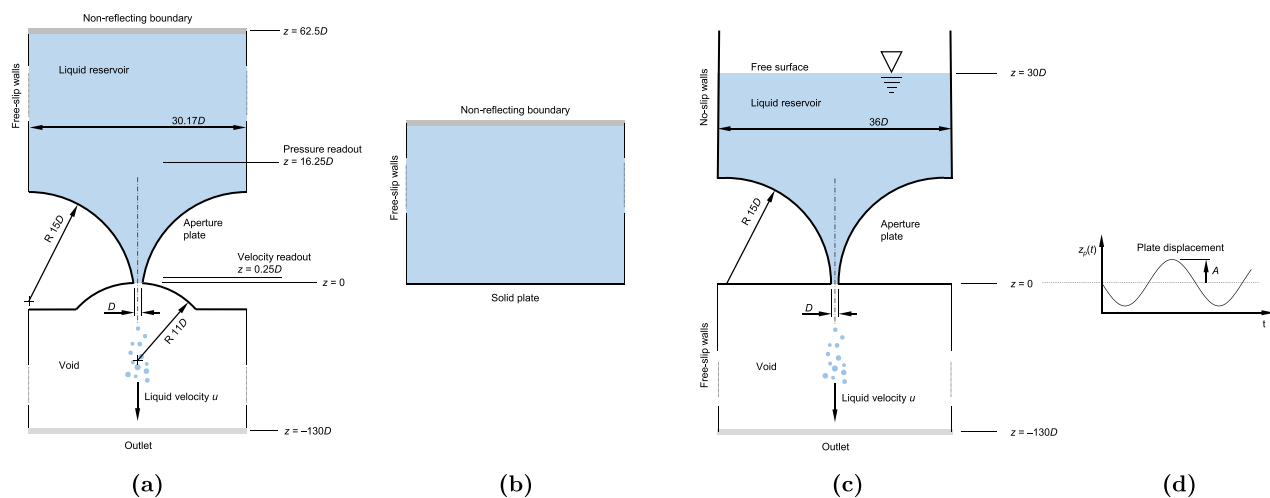
FIG. 5. Schematic diagrams of the computational models. (a) VMN with aperture, with locations for readouts of reservoir pressure and aperture exit velocity. (b) Solid plate at VMN scale without aperture. (c) Scaled-up model aperture. (d) Plate displacement $z_p(t)$ for all models, defined positive upward (into the reservoir).
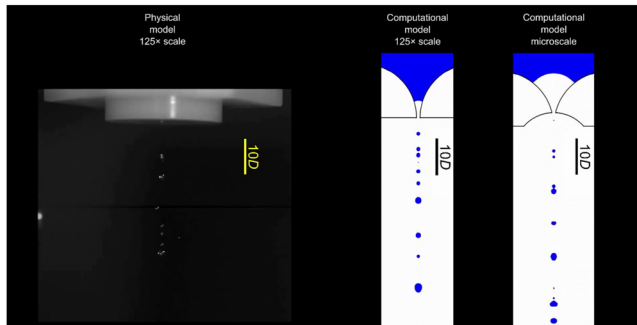
FIG. 6. Experimental image (left) and computational simulation (middle) of the large-scale model VMN aperture, with computational simulation (right) of the microscale VMN aperture. The scale bar indicates 10 aperture diameters. Multimedia available online.

accurately models the physical compressibility of liquid water across a wide range of pressure.[31] For the microscale VMN, as discussed in Sec. II A, the physical speed of sound $c_0 = 1480$ m/s is used. For the large-scale model, the flow is practically incompressible and it is not necessary to resolve acoustic waves. In this case, the Tait EoS serves as a model for weak compressibility. To reduce computational cost, a lower sound speed of $c_0 = 100$ m/s is set. Tests have confirmed that results are insensitive to c_0.

V. RESULTS

Images from the large-scale model experiment and computational simulations of both the large-scale model and microscale VMN are shown in Fig. 6 (Multimedia view). Results are discussed in further detail in the following sections.

A. Experiments and computation for the large-scale model

Experimental images and computational simulations of flow from the large-scale model VMN aperture are shown in Fig. 7 and in the multimedia linked to Fig. 6. Results are for the baseline operating condition of $A = 1.25\,\mu$m, $\theta = 105°$, $\sigma = 0.0735\,\text{Nm}^{-1}$, and $\mu = 10^{-3}\,\text{Nm}^{-2}$ s. The phase of each image is shown as $t^* = t/T \mod 1$, where T is the period, and scales are shown in units of aperture exit diameter D. The experimental images have been processed with a Sobel edge detection filter. The inherent instability of the jet breakup flow leads to significant cycle-to-cycle variation within both the experiments and the computations, and consequent timing differences between the experiments and computations. The images are selected from various cycles to illustrate similarity of structures and mechanisms observed in both computation and experiments. At $t^* = 0.185$ and 0.280 in experiment and computation, respectively, we see a jet emerging from the aperture, and isolated drops downstream of diameter of order D. At $t^* = 0.397, 0.395$, a slender jet extends from the aperture to a large drop approximately $15D$ downstream, with a separate smaller drop a little further downstream. At $t^* = 0.905, 0.950$, a column of liquid has just broken up into drops with long slender tails. Noting the difficulty of achieving exact agreement due to the instability and variability of the process, the computational
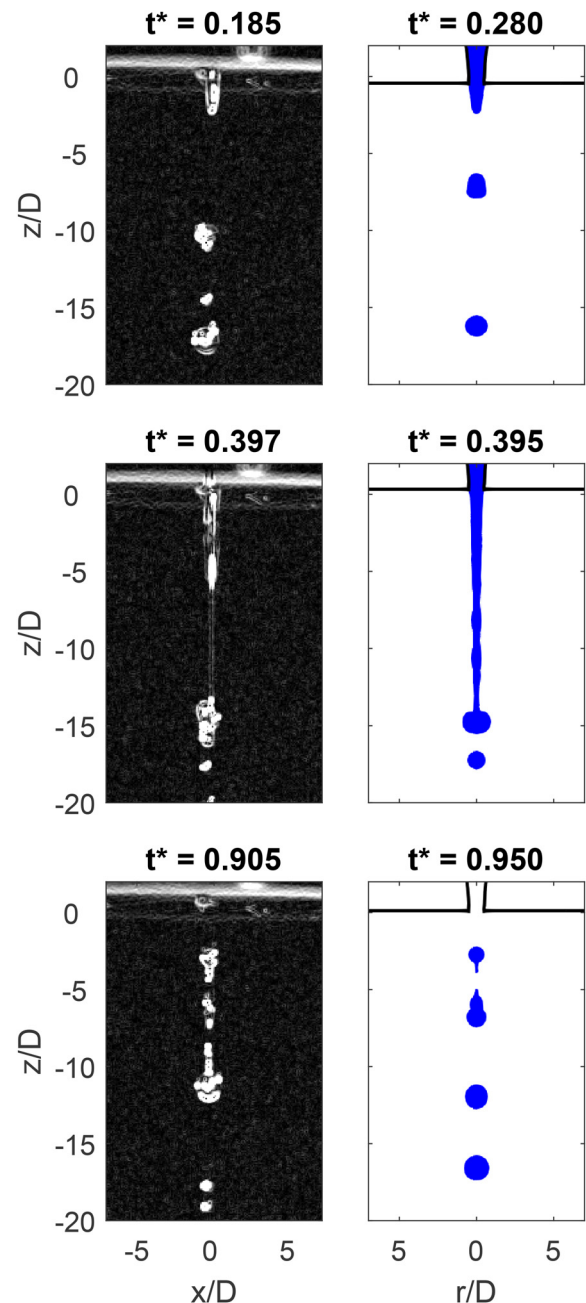

FIG. 7. Comparison of experimental images (left) and computational simulations (right) of the large-scale model VMN aperture.

model is capable of predicting the gross structure and morphology of the flow.

B. Resolution sensitivity in the computational model

Simulations of the microscopic aperture were conducted for particle distributions of 8, 16, and 32 particles across the aperture diameter. Results are shown in Fig. 8. There are significant discrepancies
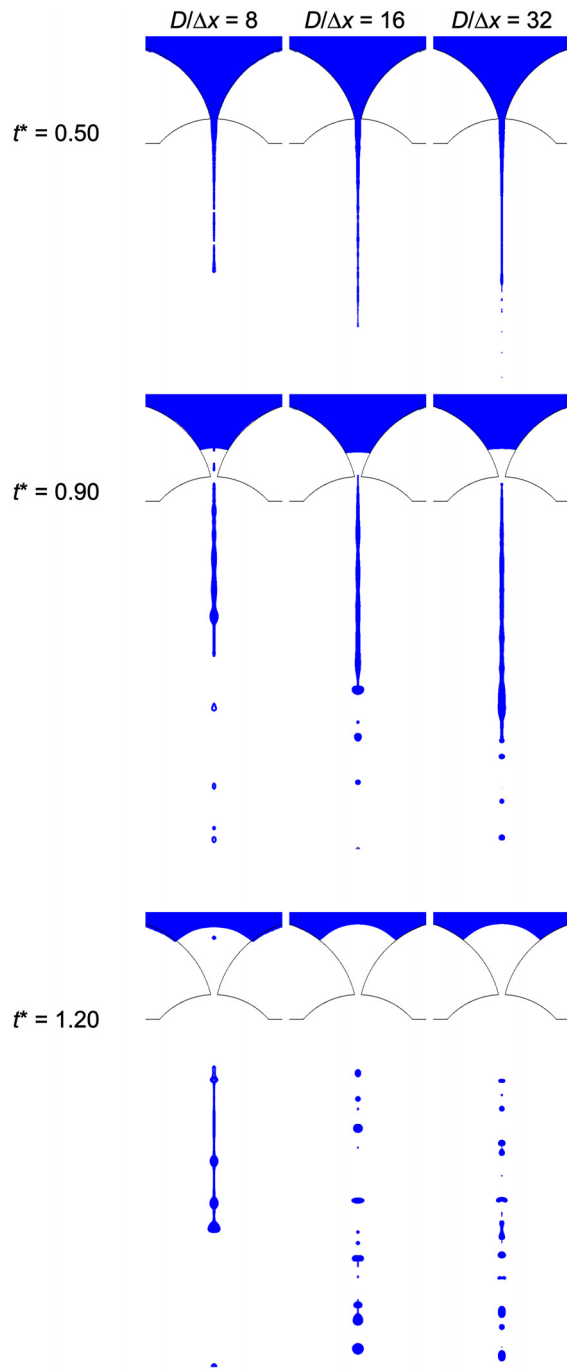
FIG. 9. (a) Dimensionless pressure $p^* = p/(\rho A\omega c_0)$ at $z^* = z/D = 16.25$ in a reservoir driven by an oscillating closed plate, along with dimensionless prescribed plate velocity $\dot{z}_p^* = \dot{z}_p/(A\omega) = -\cos(2\pi t^*)$; (b) pressure fields at selected instants. Note that the color scale for pressure varies with time, but the range remains constant.

considered sufficient for the present work and is used throughout the remainder of the work.

C. Mechanism of operation

In this section, we illustrate and discuss the mechanism of droplet generation in the microscale system, with results from the baseline case. The process is considered in two stages: pumping from the reservoir through the aperture, and the downstream formation of a jet and droplets.

1. Pumping

To investigate the pressurization of the reservoir by plate vibration, without the complicating effects of aperture flow, simulations were carried out of an oscillating solid plate with no aperture. As shown in Fig. 5(b), the reservoir has a flat bottom wall, but dimensions and operating conditions are otherwise the same as for the model of the microscopic VMN aperture shown in Fig. 5(a). Time-varying pressure distributions are shown in Fig. 9. As discussed in Sec. II A, the VMN is expected to operate in a regime of compressible flow dominated by acoustic waves. In one-dimensional compressible flow driven by a moving plate, momentum conservation requires that a plate velocity increment $\mathrm{d}u_p$ results in a pressure increment $\mathrm{d}p = \rho c\,\mathrm{d}u_p$. In the present case, with approximately constant density $\rho \simeq \rho_0$ and sound speed $c \simeq c_0$, and plate velocity $u_p = \dot{z}_p = -A\omega \cos \omega t$ (positive upward, i.e., into the reservoir), the expected pressure on the plate is $p(t) = p_a + \rho_0 c_0 \int \mathrm{d}u_p = -\rho_0 A\omega c_0 \cos \omega t$. In Fig. 9 and other results, pressure is non-dimensionalized as $p^* = (p(t) - p_a)/(\rho_0 A\omega c_0)$, where p_a is atmospheric or background pressure, and the denominator is the maximum pressure in the 1D theory. This dimensionless theoretical pressure is then simply $p^* = -\cos(2\pi t^*)$ and is equal to the dimensionless plate velocity $\dot{z}_p^* = \dot{z}_p/(A\omega) = -\cos \omega t = -\cos(2\pi t^*)$.

Results in Fig. 9 show that the pressure closely follows the sinusoidal plate velocity and the theoretical profile. At $t^* = 0.25$, the pressure decreases with height above the plate, consistent with propagation of a compression wave from the plate. The converse is true at $t^* = 0.75$. On the time scale of plate oscillation, the pressure field in

FIG. 8. Comparison of computed liquid free surfaces for three spatial resolutions at three time points.

between the $D/\Delta x = 8$ and $D/\Delta x = 16$ cases in terms of the jet length, timing of breakup, and number and size of droplets formed. There is closer agreement between $D/\Delta x = 16$ and $D/\Delta x = 32$ in terms of the distribution and size of droplets. Resolution of $D/\Delta x = 16$ is
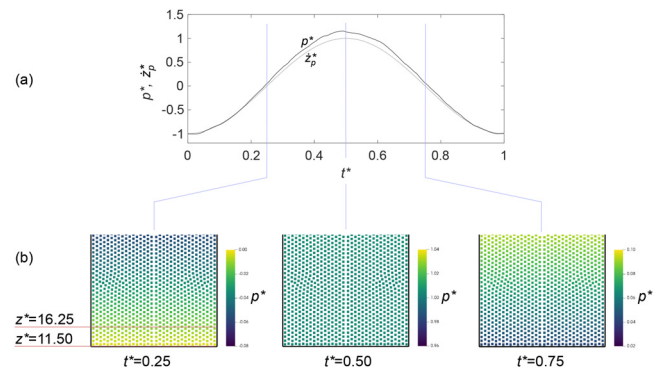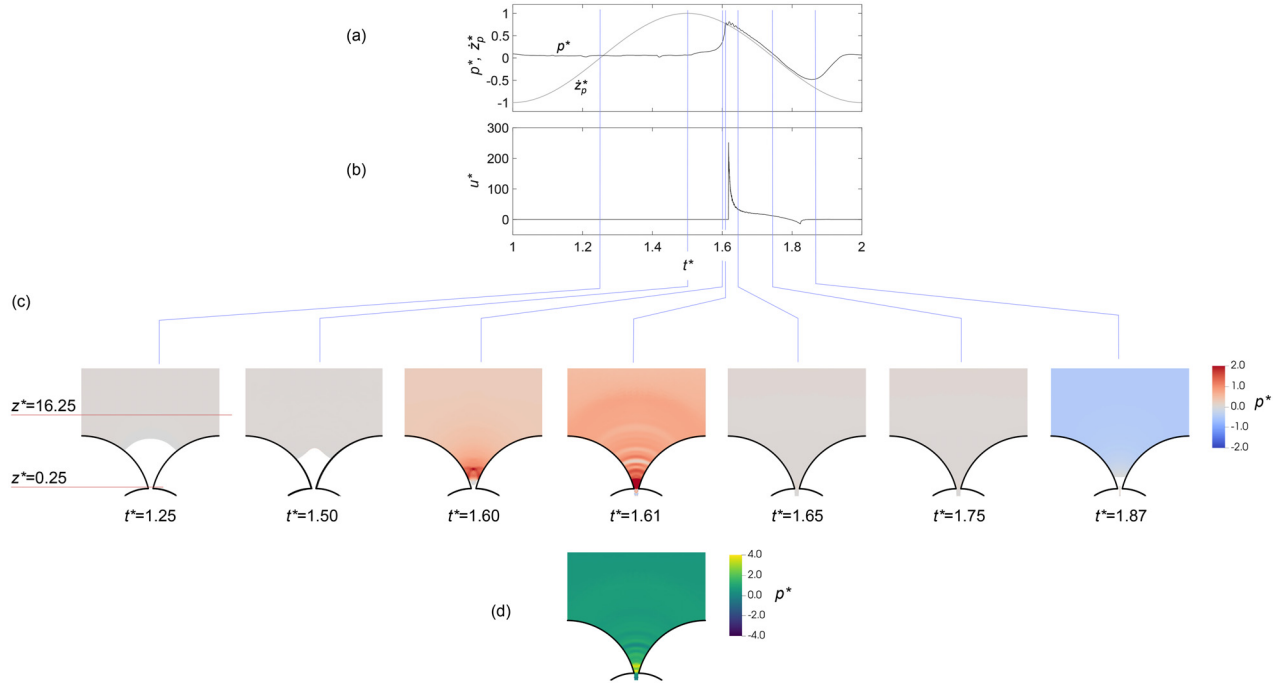
FIG. 10. Computational results for the microscopic VMN aperture and reservoir. (a) Dimensionless pressure $p^* = p/(\rho A\omega c_0)$ at $z^* = z/D = 16.25$ in a reservoir driven by an oscillating aperture plate with dimensionless prescribed plate velocity $\dot{z}_p^* = \dot{z}_p/(A\omega) = -\cos(2\pi t^*)$ (positive up); (b) dimensionless axial velocity $u^* = u/(A\omega)$ (positive down) in the aperture at $z^* = 0.25$; (c) pressure fields at selected instants; and (d) pressure field at $t^* = 1.61$ on an extended color scale.

the reservoir is strongly non-uniform and unsteady due to compressibility. This is due to the relatively long transit time of acoustic waves.

The pressure field in the full VMN model, with aperture, is shown in Fig. 10. At $t^* = 1.25$, $\dot{z}_p = 0$ and $p^* \approx 0$, i.e., pressure is atmospheric. At $t^* = 1.50$, when pressure is maximum on the solid plate, the reservoir is now pressurized only slightly to $p^* \approx 0.05$. At this stage, atmospheric pressure dominates the reservoir because of the large free surface in the upper region of the aperture. The small positive pressure drives liquid

into the aperture and the free surface shrinks as it advances into the converging aperture. At $t^* \gtrsim 1.6$, the free surface area is just slightly larger than the exit area. Approximately 99.8% of the projected plate area is now in contact with liquid in the reservoir, and the upward-moving plate's compressive action begins to dominate the reservoir pressure. At $t^* = 1.61$, just above the aperture plate, at $z^* = 16.25$, pressure jumps to the 1D solution $p(t) = p_a - \rho_0 A\omega c_0 \cos\omega t$ or $p^* = -\cos(2\pi t^*)$, equal to plate velocity $\dot{z}_p^*$. Meanwhile, much higher pressure ($p^* > 3$) occurs inside the aperture as the unsteady flow advances into the converging duct. After pressure drops below atmospheric, there is a brief period of reverse flow as liquid is ingested back into the aperture. Reservoir pressure remains close to the theoretical value, following the plate velocity, until $t^* \simeq 1.87$, when the free surface retreats into the aperture and atmospheric pressure dominates again.

The large-scale model aperture undergoes a fundamentally different pumping mechanism, as shown in Fig. 11. Pressure just above the plate is in phase with the plate acceleration rather the velocity. This is consistent with the theoretical model of a quasi-steady hydrostatic pressure distribution due to vertical acceleration of the whole fluid column driven by the oscillation of the aperture plate. The pressure oscillation about the mean closely follows the expected hydrostatic value $\rho_0 A\omega^2(H-z)\sin(2\pi t/T)$, where $H-z$ is the depth of the pressure readout plane below the reservoir free surface.

FIG. 11. Computational results for the large-scale model aperture: (a) dimensionless pressure $p^* = (p - \bar{p})/(\rho_0 A\omega^2(H-z))$ at $z^* = z/D = 16.25$, aperture plate velocity $\dot{z}_p^* = \dot{z}_p/(A\omega) = -\cos(2\pi t^*)$ (positive up), and aperture plate acceleration $\ddot{z}_p^* = \ddot{z}_p/(A\omega^2) = \sin(2\pi t^*)$ (positive up) and (b) dimensionless axial velocity $u^* = u/(A\omega)$ (positive down) in the aperture at $z^* = 0.25$.

2. Jet and droplet formation

Visualisations of computed flow downstream of the microscale VMN aperture are shown in Fig. 12, and in the multimedia linked to
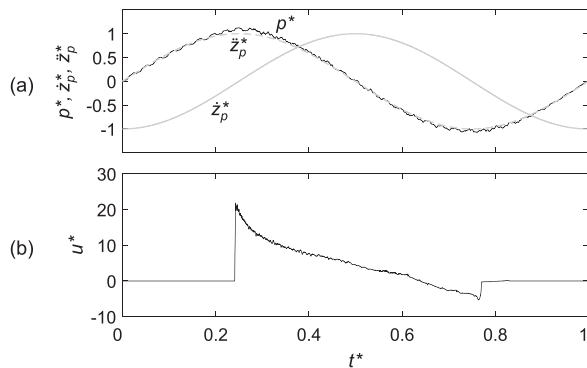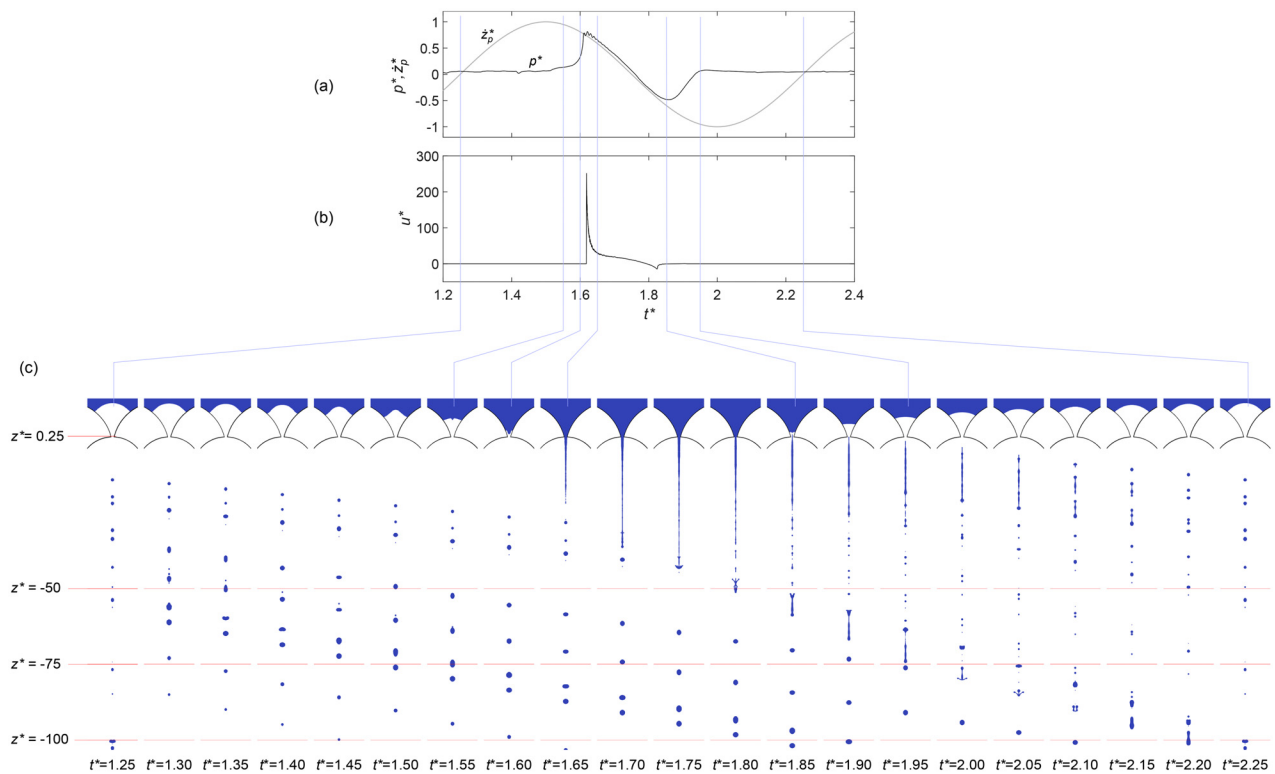
FIG. 12. Computational results for flow from the microscopic VMN aperture at baseline operating conditions. (a) Dimensionless pressure $p^* = p/(\rho A \omega c_0)$ at $z^* = z/D = 16.25$ in the reservoir dimensionless aperture plate velocity $\dot{z}_p^* = \dot{z}_p/(A\omega) = -\cos(2\pi t^*)$; (b) dimensionless axial velocity $u^* = u/(A\omega)$ in the aperture at $z^* = 0.25$; and (c) visualization of liquid at intervals of 1/20 of a cycle.

Fig. 6. At the first instant shown, $t^* = 1.25$, the plate is at its lowest position and zero velocity, and gauge pressure in the reservoir is close to zero. Droplets from the previous cycle are downstream of the aperture. Up to $t^* \simeq 1.5$, the free surface in the aperture remains large, and consequently, the reservoir pressure remains close to atmospheric. Between $t^* \simeq 1.55$ and $t^* \simeq 1.65$, liquid accelerates into the aperture and free surface area decreases. Pressure rapidly rises to and then follows the sinusoid expected from compressible 1D theory. By $t^* = 1.65$, liquid has emerged from the exit under influence of the rapidly increasing reservoir pressure. Velocity at the aperture exit [Fig. 12(b)] is initially high and declines rapidly, so that the new jet is much faster than trailing droplets from the preceding cycle. By $t^* = 1.70$, the jet has collided with droplets.

Perturbations in the jet's diameter appear and grow from early stages. By $t^* = 1.80$, the perturbations have grown large enough to pinch off the jet, with breakup appearing around $z^* = z/D \simeq -40$. For the remainder of the cycle, fragments of the original jet undergo further breakup events and/or contract axially and tend toward spherical droplets on the order of the aperture exit diameter. Smaller droplets are also formed as satellite droplets from breakup events. This is consistent with Rayleigh–Plateau capillary instability. The large volume of liquid formed by jet–droplet collision at $z^* \simeq -50$, $t^* \simeq 1.80$ elongates and undergoes further breakup, but also collides and merges with other older slower droplets.

As shown in Fig. 12, dimensionless aperture exit velocity ranges from -18 to 285. The mean exit velocity in forward flow over multiple cycles is $u^* \simeq 13$, giving $We \simeq 9$, $Re_D \simeq 51$, and $Oh \simeq 0.0583$. According to Eq. (1), the fastest-growing wavelength is $\lambda_0/D = 4.710$ and the corresponding droplet diameter is $1.92\,D$. This is somewhat larger than most drops visualized in Fig. 12, which are similar in diameter to the aperture exit. (Further analysis of droplet size will be presented later.) This suggests that the nozzle flow perturbs the jet at wavelengths shorter than the fastest-growing wavelengths.

At $t^* = 1.75$, the plate motion reverses direction and reservoir pressure goes negative. The jet, with its downward momentum, thins near the aperture exit and detaches at $t^* \simeq 1.85$. A new free surface is formed just inside the aperture and begins to recede upwards. As it does so, its area increases, and the reservoir pressure again deviates from $p^* = -\cos(2\pi t^*)$ and returns to atmospheric.

D. Jet–droplet collisions

Many jet–droplet collisions are apparent in the results, with Weber numbers (based on relative velocity) typically on the order of 300. An example appears between $t^* = 1.65$ and $t^* = 1.70$ at $z^* \simeq -35$ in Fig. 12. This particular event results in coalescence to form a liquid column that undergoes strong dynamic deformations and breaks up some time later ($t^* \simeq 2.00$). In the computational model, collisions are
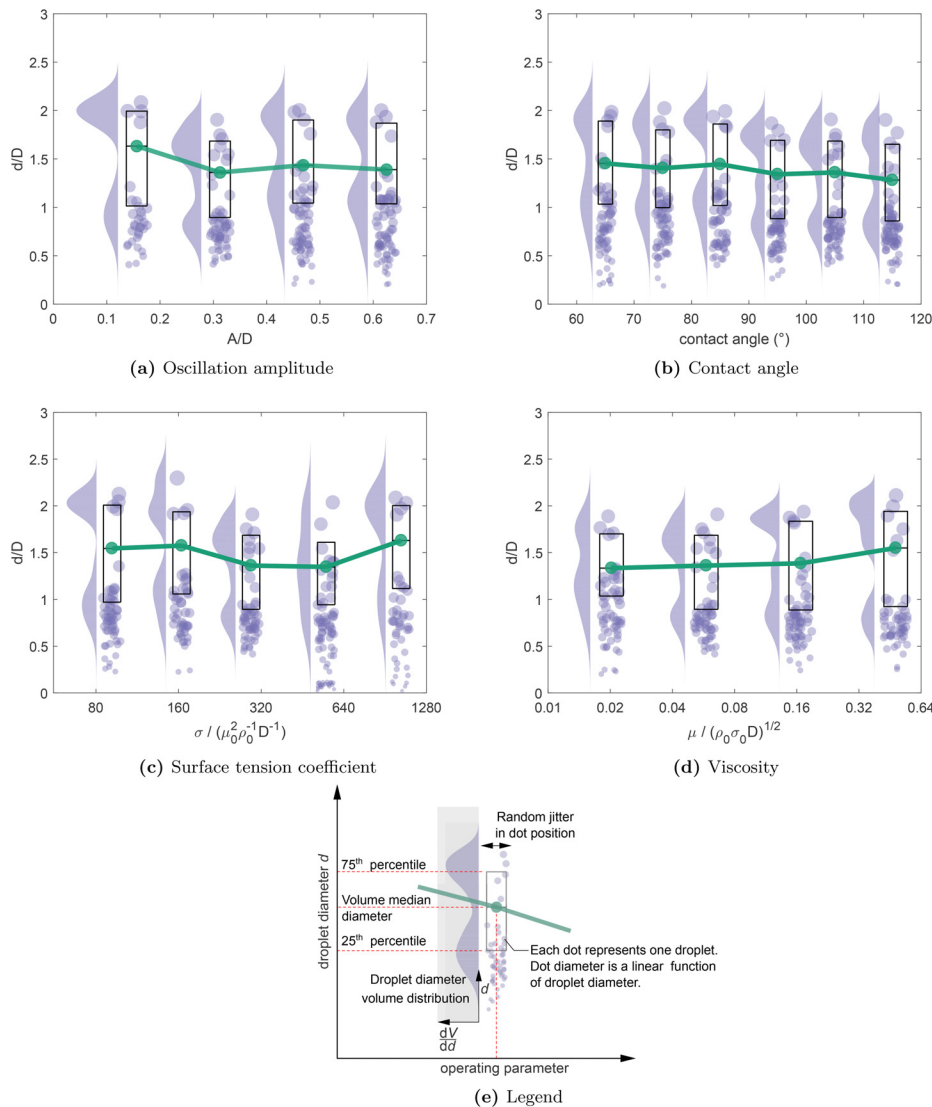
(a) Oscillation amplitude

(b) Contact angle

(c) Surface tension coefficient

(d) Viscosity

FIG. 13. Effect of non-dimensionalized operating parameters on droplet size distribution over 4 cycles at $-z/D = 50$. Operating parameters are held at the baseline condition of $A/D = 0.3125$, $\theta = 105°$, $\sigma_0 = 0.0735\,\mathrm{Nm}^{-1}$ $(\sigma/(\mu_0^2\rho_0^{-1}D^{-1}) = 294)$, and $\mu_0 = 10^{-3}\,\mathrm{Nm}^{-2}\,\mathrm{s}$ $(\mu/(\rho_0\sigma_0D)^{1/2} = 0.0583)$, corresponding to water at nominal operating conditions, except for the independent variable on the x axis in each study. Droplet diameter volume distributions are kernel density estimates with a normal kernel, and are plotted on the same scale in every plot. The visualization is based on the raincloud plot concept of Allen et al.[35]

(e) Legend

constrained by the enforced axisymmetry and always result in coalescence. In the large-scale experimental model, on the other hand, we have observed many collisions resulting in off-axis scattering of small drops.

The literature documents extensive experimental work on droplet–droplet collisions with diameter ratios up to 2. The following quantitative findings from literature should be applied with caution in interpretation of the present work, which involves droplets impacted by jets or liquid columns of similar diameter but much higher mass. Ashgriz and Poo[32] showed droplet–droplet coalescence is unlikely at $We = 100$ (the upper limit in that study), especially for on-axis or nearly on-axis collisions of equal-sized droplets. Qian and Law[33] showed evidence that the gas phase plays a role in droplet bouncing, but only for We up to about 10. This is not relevant for the present simulations, where collision Weber numbers are much higher. Pan et al.[34] identified a "fingering and separation" regime for on-axis equal droplets at higher Weber numbers, $250 \lesssim We \lesssim 300$. In this type of collision, droplets form a disk-like shape before contracting radially

and extending axially into a perturbed liquid column, which then breaks up into a few droplets of diameter similar to the original pair. This is similar to the process seen at $1.65 < t^* < 2.00$ in Fig. 12. Pan et al. reported further regimes for $We \gtrsim 300$, in which the droplets again merge into a disk, which is subject to a non-axisymmetric instability, and rapidly disintegrates into many small droplets.

Thus, our model displays jet–droplet collision behaviors, which are consistent with *droplet*–droplet behavior in the literature (noting the caveats above). However, the model is likely to be excluding some non-axisymmetric high-We dynamics, and consequently underpredicting the formation of smaller droplets.

E. Droplet size and effect of operating conditions

Simulations were carried out for a range of oscillation amplitude, contact angle, surface tension coefficient, and viscosity. Unphysical extreme values of viscosity and surface tension coefficient were
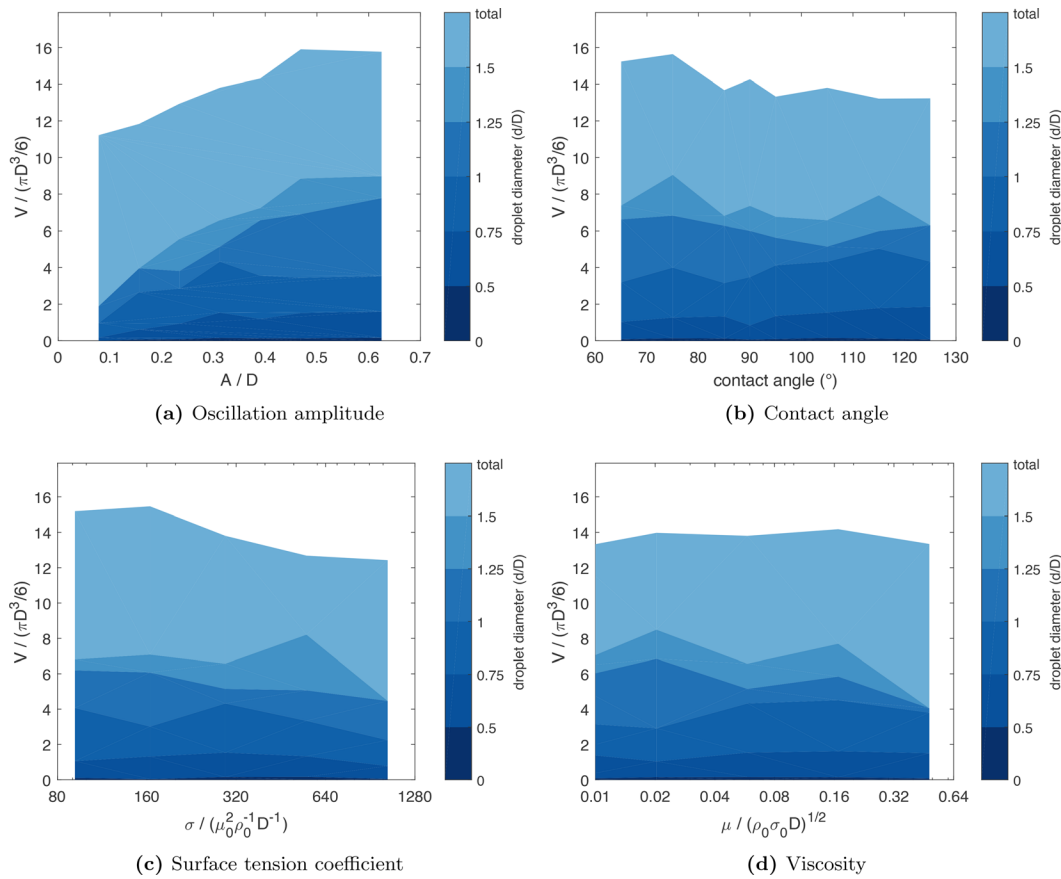
FIG. 14. Effect of non-dimensionalized operating parameters on aerosol volume in various droplet diameter bands. The y axis of each plot shows volume per oscillation cycle passing a sample line at $-z/D = 50$, normalized to the volume of a spherical droplet of diameter equal to aperture diameter. Operating parameters are held at the baseline condition of $A/D = 0.3125$, $\theta = 105°$, $\sigma_0 = 0.0735\,\mathrm{Nm^{-1}}$ ($\sigma/(\mu_0^2\rho_0^{-1}D^{-1}) = 294$), $\mu_0 = 10^{-3}\,\mathrm{Nm^{-2}\,s}$ ($\mu/(\rho_0\sigma_0 D)^{1/2} = 0.0583$), except for the variable parameter in each study.

included in the test series. Droplet diameter distributions are shown in Fig. 13 for four test series, in each of which one operating parameter was varied. Total volume of aerosol generation is shown in Fig. 14.

The baseline case described above appears in each series, for example, as $A/D = 0.3125$ in the amplitude series [Fig. 13(a)]. Volume median diameter (VMD) of droplets is $1.35D$ in the baseline case. Over four cycles, just seven droplets are larger than that median, accounting for half of total volume. There are two distinct clusters of particle size, with peaks in the volume-weighted droplet diameter distribution at *1.60D* and *0.78D*. Each peak is associated with about half of the total aerosolized volume, but the lower diameter peak represents a much larger number of droplets. This split appears at nearly all operating conditions. Data such as Fig. 12 suggest that the larger drops are formed by collision of the jet with older drops, while drops of the diameter of the aperture exit and less are formed by primary breakup.

Oscillation amplitude A is by far the most influential operating parameter. VMD decreases slightly with increasing amplitude, up to $A/D = 0.3125$ [Fig. 13(a)]. However, the volume of aerosol generated increases strongly with amplitude [Fig. 14(a)]. At low amplitude, this occurs across all droplet size bands, but for $A/D \gtrsim 0.4$, most of the

growth is in the $1 \lesssim d/D \lesssim 1.25$ droplet size band. VMD and total volume decline slightly as contact angle increases from hydrophilic to hydrophobic regimes [Figs. 13(b) and 14(b)]. As surface tension is increased [Figs. 13(c) and 14(c)], droplet size declines, consistent with the expectation from Eq. (1) for viscous Plateau–Rayleigh breakup. There is a minimum for both the VMD and the interquartile range of droplet size around the surface tension coefficient of water ($\sigma_0 = 0.0735$ N m^{-1}, $\sigma_0\rho_0 D\mu_0^{-2} = 294$) with a notable peak for droplet diameter at $d/D \simeq 0.75$ at that condition. At higher surface tension coefficients (which do not represent real liquids of interest), there is a sharp decline in production of smaller droplets in the $d/D \lesssim 1.5$ range. As viscosity increases [Figs. 13(d) and 14(d)], there is a trend of gradually increasing droplet size, which again is consistent with viscous Plateau–Rayleigh theory.

VI. CONCLUSIONS

In this study, we conducted computational and experimental simulations of flow through a microscopic aperture of a vibrating mesh nebulizer (VMN). The experimental model was scaled up to approximately preserve Reynolds and Weber numbers. The computational

model, based on a meshless Lagrangian FVPM method to simplify treatment of complex free surfaces, was validated by comparison with the scaled-up experiment, showing that the model can correctly predict the structure of the flow.

Liquid in the reservoir is pressurized by upward acceleration of the aperture plate, pumping flow through the aperture to form a jet. The time and length scales are such that acoustic compression waves are responsible for local transient pressurization of the VMN reservoir. In the large-scale model, on the other hand, a quasi-equilibrium hydrostatic pressure is established in the reservoir. The jet through the aperture is subject to Plateau–Rayleigh capillary instability and breaks up into droplets of diameter on the order of the aperture diameter. Smaller droplets are formed as satellites in breakup, and some larger droplets are formed by collisions.

Oscillation amplitude is the most significant operating parameter investigated, with higher amplitude leading to higher aerosol volume in all droplet sizes, and smaller droplet volume median diameter (VMD). High amplitude particularly favors droplets just above aperture diameter, $1.00 < A/D \leq 1.25$. VMD decreases by up to 10% as surface tension is increased (up to the value of water) or viscosity is decreased, consistent with literature on the Plateau–Rayleigh instability. VMD declines similarly as contact angle increases. These findings suggest that liquid formulations of low viscosity and high surface tension, and hydrophobic aperture surfaces, are desirable to achieve low droplet sizes conducive to deep lung delivery. This modeling framework, validated against a large-scale experimental single-aperture model, may be used further to investigate effects of aperture geometry as well as oscillation parameters and liquid properties, to guide the design of future VMNs.

The computational model is axisymmetric and single-phase, limiting its ability to capture bouncing or separation of droplets in collisions, whereas the scaled-up experiment shows non-axisymmetric release of droplets from collisions. This likely results in some computational overprediction of droplet diameters. A 3D multiphase model will be developed in future work. Pumping conditions are modeled in the present work by an approximation of locally uniform plate displacement. The effect of realistic plate oscillation modes on pumping through the apertures could be investigated in future with a 3D model of flow in the reservoir, and coupling to a computational model for plate deformation. Finally, surface roughness and dynamic wetting effects has not been considered in the present work and may be incorporated in future models.

ACKNOWLEDGMENTS

AUTHOR DECLARATIONS
Conflict of Interest

Yes, R.M.L. is an employee of Aerogen Ltd.

Author Contributions

Mohsen H. Moghimi: Conceptualization (equal); Data curation (equal); Formal analysis (equal); Investigation (lead); Methodology (lead); Software (equal); Validation (equal); Visualization (equal); Writing – original draft (equal); Writing – review & editing (equal). **José A. Monterrubio López:** Conceptualization (equal); Investigation (lead); Methodology (equal); Visualization (equal); Writing – original draft (equal). **Ciarán Guy:** Investigation (equal); Methodology (equal). **Gerard M. O'Connor:** Investigation (equal); Methodology (equal); Resources (equal); Supervision (equal); Writing – review & editing (equal). **Ronan MacLoughlin:** Conceptualization (lead); Formal analysis (equal); Funding acquisition (lead); Investigation (equal); Methodology (equal); Project administration (equal); Resources (equal); Supervision (equal); Writing – review & editing (equal). **Nathan J. Quinlan:** Conceptualization (lead); Data curation (equal); Formal analysis (equal); Funding acquisition (lead); Investigation (lead); Methodology (equal); Project administration (lead); Resources (equal); Software (equal); Supervision (lead); Validation (equal); Visualization (equal); Writing – original draft (lead); Writing – review & editing (equal).

DATA AVAILABILITY

The data that support the findings of this study are available from the corresponding author upon reasonable request.

REFERENCES

[1] F. Réminiac, L. Vecellio, R. Mac Loughlin, D. Le Pennec, M. Cabrera, N. H. Vourc'h, J. B. Fink, and S. Ehrmann, "Nasal high flow nebulization in infants and toddlers: An in vitro and in vivo scintigraphic study," Pediatr. Pulmonol. **52**(3), 337–344 (2017).

[2] R. B. Dunne and S. Shortt, "Comparison of bronchodilator administration with vibrating mesh nebulizer and standard jet nebulizer in the emergency department," Am. J. Emergency Med. **36**(4), 641–646 (2018).

[3] S. Wu, J. Huang, Z. Zhang, J. Wu, J. Zhang, H. Hu, T. Zhu, J. Zhang, L. Luo, P. Fan et al., "Safety, tolerability, and immunogenicity of an aerosolised adenovirus type-5 vector-based COVID-19 vaccine (Ad5-nCoV) in adults: Preliminary report of an open-label and randomised phase 1 clinical trial," Lancet Infect. Dis. **21**(12), 1654–1664 (2021).

[4] V. C. Galindo-Filho, M. E. Ramos, C. S. Rattes, A. K. Barbosa, D. C. Brandão, S. C. S. Brandão, J. B. Fink, and A. D. de Andrade, "Radioaerosol pulmonary deposition using mesh and jet nebulizers during noninvasive ventilation in healthy subjects," Respiratory care **60**(9), 1238–1246 (2015).

[5] J. C. Dubus, L. Vecellio, M. De Monte, J. B. Fink, D. Grimbert, J. Montharu, C. Valat, N. Behan, and P. Diot, "Aerosol deposition in neonatal ventilation," Pediatr. Res. **58**(1), 10–14 (2005).

[6] R. J. MacLoughlin, B. D. Higgins, J. G. Laffey, and T. O'Brien, "Optimized aerosol delivery to a mechanically ventilated rodent," J. Aerosol Med. Pulm. Drug Delivery **22**(4), 323–332 (2009).

[7] A. B. Watts, J. T. McConville, and R. O. Williams III, "Current therapies and technological advances in aqueous aerosol drug delivery," Drug Dev. Ind. Pharm. **34**(9), 913–922 (2008).

[8] A. Arnott, M. Watson, and M. Sim, "Nebuliser therapy in critical care: The past, present and future," J. Intensive Care Soc. **25**, 78 (2024).

[9] W. von Ohnesorge, "The formation of drops by nozzles and the breakup of liquid jets (Translated by Trettel, B," Z. Angew. Math. Mech. **16**(6), 355–358 (1936). URL https://repositories.lib.utexas.edu/handle/2152/76302

[10] N. Chigier and R. D. Reitz, "Regimes of jet breakup and breakup mechanisms—physical aspects," in Recent Advances In Spray Combustion: Spray Atomization and Drop Burning Phenomena, edited by K. K. Kuo (AIAA, 1996).

[11] S. P. Lin and R. D. Reitz, "Drop and spray formation from a liquid jet," Annu. Rev. Fluid Mech. **30**(1), 85–105 (1998).

[12]B. Trettel, "Reevaluating the jet breakup regime diagram," *Atomization and Sprays* (Begel House Inc., 2020), Vol. 30. URL https://www.dl.begellhouse.com/journals/6a7c7e10642258cc,0ca27cd23c7051a0,6f72c56a3e60307d.html.

[13]L. Rayleigh, "On the instability of jets," Proc. London Math. Soc. **1**(1), 4–13 (1878).

[14]J. Eggers, "Nonlinear dynamics and breakup of free-surface flows," Rev. Mod. Phys. **69**(3), 865 (1997).

[15]D. Violeau and B. D. Rogers, "Smoothed particle hydrodynamics (SPH) for free-surface flows: Past, present and future," J. Hydraul. Res. **54**, 1–26 (2016).

[16]N. J. Quinlan, "Extensions of the meshless finite volume particle method (FVPM) for static and dynamic free-surface flows," Comput. Fluids **177**, 33–45 (2018).

[17]D. Hietel, K. Steiner, and J. Struckmeier, "A finite volume particle method for compressible flows," Math. Models Methods Appl. Sci. **10**, 1363–1382 (2000).

[18]M. Junk, "Do finite volume methods need a mesh?," in *Meshfree Methods for Partial Differential Equations*, edited by M. Griebel (Springer, 2003), pp. 223–238.

[19]R. Keck and D. Hietel, "A projection technique for incompressible flow in the meshless finite volume particle method," Adv. Comput. Math. **23**, 143–169 (2005).

[20]N. J. Quinlan, L. Lobovský, and R. M. Nestor, "Development of the meshless finite volume particle method with exact and efficient calculation of interparticle area," Comput. Phys. Commun. **185**, 1554 (2014).

[21]R. Nestor, M. Basa, M. Lastiwka, and N. Quinlan, "Extension of the finite volume particle method to viscous flow," J. Comput. Phys. **228**, 1733–1749 (2009).

[22]N. J. Quinlan and M. H. Moghimi, "Adaptation of the finite volume particle method for axisymmetric flows with surface tension," in *15th International SPHERIC Workshop*, edited by A. Tafuni (New Jersey Institute of Technology, 2021), pp. 97–103.

[23]M. H. Moghimi and N. J. Quinlan, "Application of finite volume particle method for axisymmetric modeling of droplet formation in dripping and Rayleigh regimes," Comput. Fluids **236**, 105321 (2022).

[24]M. McLoone and N. J. Quinlan, "Particle transport velocity correction for the finite volume particle method for multi-resolution particle distributions and exact geometric boundaries," Eng. Anal. Boundary Elem. **114**, 114–126 (2020).

[25]M.-S. Liou, "A sequel to AUSM, part II: AUSM+-up for all speeds," J. Comput. Phys. **214**, 137–170 (2006).

[26]J. Bonet and T.-S. L. Lok, "Variational and momentum preservation aspects of smooth particle hydrodynamic formulations," Comput. Methods Appl. Mech. Eng. **180**, 97–115 (1999).

[27]T. Barth and D. Jespersen, "The design and application of upwind schemes on unstructured meshes," in *AIAA 27th Aerospace Sciences Meeting* (AIAA, Reno, 1989).

[28]M. H. Moghimi and N. J. Quinlan, "A model for surface tension in the meshless finite volume particle method without spurious velocity," Comput. Fluids **179**, 521–532 (2019).

[29]M. H. Moghimi and N. J. Quinlan, "Application of background pressure with kinematic criterion for free surface extension to suppress non-physical voids in the finite volume particle method," Eng. Anal. Boundary Elem. **106**, 126–138 (2019).

[30]M. H. Moghimi, "Investigation of fluid dynamics in a vibrating mesh nebulizer using the finite volume particle method," Ph.D. thesis (Nui Galway, Ireland, 2020).

[31]R. H. Cole, *Underwater Explosions* (Princeton University Press, Princeton, 1948).

[32]N. Ashgriz and J. Y. Poo, "Coalescence and separation in binary collisions of liquid drops," J. Fluid Mech. **221**, 183–204 (1990).

[33]J. Qian and C. K. Law, "Regimes of coalescence and separation in droplet collision," J. Fluid Mech. **331**, 59–80 (1997).

[34]K.-L. Pan, P.-C. Chou, and Y.-J. Tseng, "Binary droplet collision at high Weber number," Phys. Rev. E **80**(3), 036301 (2009).

[35]M. Allen, D. Poggiali, K. Whitaker, T. R. Marshall, J. van Langen, and R. A. Kievit, "Raincloud plots: A multi-platform tool for robust data visualization," Wellcome Open Res. **4**, 63 (2021).

11 December 2025 06:06:47